Nanotechnology

Ohmic contact engineering in few-layer black Phosphorus: approaching the quantum limit

To cite this article before publication: Francesca Telesio *et al* 2020 *Nanotechnology* in press https://doi.org/10.1088/1361-6528/ab8cf4

Ohmic contact engineering in few–layer black Phosphorus: approaching the quantum limit

F. Telesio[1], G. le Gal[1], M. Serrano-Ruiz[2], F. Prescimone[3], S. Toffanin[3], M. Peruzzini[2], and S. Heun[1]

[1] NEST, Istituto Nanoscienze–CNR and Scuola Normale Superiore, Piazza San Silvestro 12, 56127 Pisa, Italy

[2] Istituto di Chimica dei Composti Organometallici (CNR-ICCOM), Via Madonna del Piano 10, 50019 Sesto Fiorentino, Italy

[3] Istituto per lo Studio dei Materiali Nanostrutturati–CNR, Via Piero Gobetti 101, 40129 Bologna, Italy

E-mail: `francesca.telesio@nano.cnr.it`

8 April 2020

Abstract. Achieving good quality Ohmic contacts to van der Waals materials is a challenge, since at the interface between metal and van der Waals material different conditions can occur, ranging from the presence of a large energy barrier between the two materials to the metallization of the layered material below the contacts. In black phosphorus (bP), a further challenge is its high reactivity to oxygen and moisture, since the presence of uncontrolled oxidation can substantially change the behavior of the contacts. Here we study three of the most commonly used metals as contacts to bP, Chromium, Titanium, and Nickel, and investigate their influence on contact resistance against the variability between different flakes and different samples. We investigate the gate dependence of the current–voltage characteristics of field–effect transistors fabricated with these metals on bP, observing good linearity in the accumulation regime for all metals investigated. Using the transfer length method, from an analysis of ten devices, both at room temperature and at low temperature, Ni results to provide the lowest contact resistance to bP and minimum scattering between different devices. Moreover, we observe that our best devices approach the quantum limit for contact resistance both for Ni and for Ti contacts.

Supplementary Material for this article is available online

Keywords: black Phosphorus; Ohmic contacts; transfer length method; field–effect transistors

Submitted to: *Nanotechnology*

1. Introduction

Ohmic contact engineering for van der Waals materials represents a challenge in boosting the performance of any device based on these materials. This opens new fields of investigation, since at the interface between a metal and a van der Waals material, different conditions could apply, ranging from the presence of a thick tunneling barrier to metallization of the van der Waals material below the contacts, which could dramatically modify device performance [1, 2]. With graphene, many strategies have been proposed to achieve good Ohmic contacts, from creating defects by oxygen plasma to improve the adhesion with the metal [3, 4], to the engineering of one–dimensional contacts at the edge of encapsulated flakes [5]. On the other hand, in transition metal dichalcogenides, a local phase transition between the semiconducting and the metallic phase was shown to greatly improve contact resistance [6, 7, 8, 9], as did bias annealing [10]. Moreover, a local p–type doping induced by an oxygen plasma on MoS_2 has been demonstrated to induce ambipolar behavior [11], and the quality of the contacts to these materials is still improving, as demonstrated by the very recent achievement of ultraclean interfaces between transition metal dichalcogenides and In/Au contacts [12].

Black phosphorus (bP) is a layered semiconductor [13], which has been widely studied in the last few years because of the possibility to exfoliate it to very thin layers, even down to the monolayer, called phosphorene. Few–layer black phosphorus attracted great interest in the scientific community since its demonstration in 2014 [14], because of the direct band gap, tunable by layer number from 0.3 eV in the bulk to approximately 2 eV for the monolayer [15, 16]. This feature, together with a carrier mobility which reaches up to 45000 $cm^2/(Vs)$ for encapsulated few–layer bP at cryogenic temperatures [17], is very interesting among van der Waals materials, since it places bP between graphene with its semimetallic behavior and the high band gap transition metal dichalcogenides. Moreover, bP has a peculiar crystal structure, puckered in–plane, with a strong crystalline anisotropy between the armchair and the zig–zag direction. This morphological anisotropy in the plane induces a strong anisotropy of the optical and thermal transport properties [18, 19], as well as of the electronic properties, observed by magnetotransport experiments [20, 21].

The high reactivity of bP in humid air, which is much more relevant for thin layers [22], has so far been the major drawback for device applications of this material. In particular, the combined effect of oxygen and water, also in very small concentrations, is very disruptive for bP [23, 24]. Phosphorus atoms react with oxygen forming phosphorus oxides that are hygroscopic, thus the flakes gradually hydrolyze and dissolve [14]. Moreover, this process is accelerated by light [22], especially in the UV spectral region [25].

The bP/metal interface has been studied intensely in the last few years. Since bP is a semiconductor, in analogy to 3D semiconductors, the most intuitive scenario for a bP/metal interface is the formation of a Schottky barrier at the interface between the metal and the bP flake, due to the mismatch between the work function of the metal

and the electron affinity of the semiconductor [26, 27]. Theoretical efforts have been dedicated to modeling metals on both monolayer and multilayer bP in terms of work function alignment [28, 29] and by complementary band calculations with quantum transport simulations for monolayer bP [30], as well as by density functional theory [31, 32].

Experimental work focused on characterization of the Schottky barrier height [33, 34, 35] or the contact resistance [36, 37, 38, 39, 40, 41], in order to better understand the ambipolar behavior of bP field–effect transistors [15, 42, 43, 44, 45], their anisotropic transport properties [46, 47, 48], the influence of capping [49] or annealing treatments [50], or even quantum transport [51]. In these studies, the reactivity of bP was addressed by extracting as much information as possible from the same device, for example the contact resistance for different flake thicknesses using a stepped flake [43], or by depositing contacts of two different metals on the same bP channel [36].

Our aim is complementary to such studies: we investigate if the choice of the contact metal has a sufficiently strong influence to be robust against the variability among different factors such as different flakes (with different crystallographic orientations with respect to the source–drain direction) or different fabrication batches, and thus we compare results over different transistors for each metal. The focus is on lowering the contact resistance. We discuss our results in comparison with previous studies both on contact resistance [36, 42, 44, 51, 52, 53] and on Schottky-barrier height [30, 31, 32, 33]. Moreover, we show a correlation of contact resistance with carrier concentration in bP, an information which was still missing in literature and which allows comparison with other 2D materials [9]. We chose Chromium, Titanium, and Nickel for the present study, since these transition metals present a good adhesion on SiO_2 and thus they are commonly used as adhesion layers for gold electrodes.

As a first estimate of the band alignment of the metal with the semiconductor, the Schottky–Mott approximation [27] can be used to determine the Schottky barrier height (SBH). Since bP is p–type, the SBH for holes (Φ_p) is defined as $\Phi_p = E_g - (\Phi_m - \chi)$, where Φ_m is the metal work function, χ the electron affinity of the semiconductor, and E_g the semiconductor band gap. The metals chosen have different work functions, in particular $\Phi_{Ni} \approx 5.0$ eV [36], $\Phi_{Cr} \approx 4.5$ eV [54], and $\Phi_{Ti} \approx 4.3$ eV [1], which are thus expected to produce different band alignments with bP ($\chi_{bP} \approx 4.4$ eV) [55]. From this simple rule, we would expect Ni to have the best band alignment, while Ti the worst. However, it is well known that at the interface between a metal and a semiconductor more complex phenomena can arise, leading to a Fermi level pinning [56] and deviations from the Schottky–Mott rule. The presence of Fermi level pinning has already been suggested and studied theoretically for few–layer bP [57], and it has been as well investigated experimentally [34]. What is observed for bP [34] (and what is generally observed in semiconductors) is a combination of Schottky–Mott barrier and Fermi level pinning.

2. Methods

Substrates of B–doped Si, with 300 nm thermal SiO_2, were pre–patterned by optical lithography with a grid of markers to allow flake identification. bP (prepared following a published procedure [58]) was exfoliated on these substrates. The samples were then immediately coated with a bilayer of MMA/PMMA which acts both as a protective layer for the bP and as a positive resist for electron beam lithography (EBL). After the EBL step, we performed a mild oxygen plasma. This step allows to obtain more stable contacts for two reasons: first of all, it removes the organic residues of the EBL resist after development, and furthermore, it introduces in a controlled way a thin oxide layer on the bP flake, which makes the samples more homogeneous and increases the quality of the interface [59].

Metal evaporation was performed next. We evaporated 10 nm of the selected metal, plus an overlayer of 100 nm gold. After metal evaporation, the samples underwent a 15 minutes lift–off in hot acetone. Again a bilayer of MMA/PMMA was spun onto the chips, to prevent degradation of the flakes during measurements. This coating protects the bP flakes [60, 61] and improves the field–effect transistor (FET) quality by tuning the SBH, as reported in a recent study [49].

For electrical transport measurements, the samples were bonded to a 16–pin dual–in–line chip carrier using Au wire. The transport properties were measured under vacuum ($p < 10^{-4}$ mbar) in a custom–made insert, equipped with a diode for temperature measurement. The leakage current though the gate was measured during gate loops and always found to be negligible. Atomic force microscopy (AFM) measurements were performed with a Bruker Dimension Icon AFM, in peak force mode. Data analysis was performed with the WSxM software [62]. Further details on sample fabrication and measurements are provided in the Supplementary Material.

3. Results and Discussion

3.1. Device geometry and sample preparation

The transfer length method (TLM) is one of the most frequently used methods to evaluate contact resistance [26]. It consists in measuring the two–terminal resistance (R_2) for various contact distances (Figure 1(a)). The resistance measured in two–probe configuration is the series resistance of the two contacts and the channel. Assuming that all contacts between the metal and the bP flake of the device have the same resistance R_C, R_2 can be expressed as a function of the distance d between the contacts, as $R_2 = 2 \cdot R_C + (d/W) \cdot R_S$, where $(d/W) \cdot R_S$ is the resistance of the bP channel, R_S the sheet resistance of the flake, and W its average width. We can thus extract R_C and R_S from a linear fit of R_2 vs. d. In order to compare flakes of different width, we have to normalize the contact resistance R_C to the flake width W.

Our aim is to investigate whether a general trend in contact resistance to bP is observed despite the scattering induced by possible residual oxidation and

inhomogeneities. Therefore, the bP flakes used for this experiment, despite being from the same source, were selected from different crystals of different batches. Two different exfoliation protocols, one in a glove box and one in a glove bag, are used. For the devices, elongated bP flakes were chosen, which showed a regular shape and an optical contrast typical of flakes of few tens of nanometers thickness. Several parallel contacts were designed on the flakes by EBL, at nominal distances d_1 ranging from 600 nm to 1 μm, depending on flake length L (Figure 1(a)). Overall, 10 devices were realized and characterized, both at room temperature and at low temperature. An optical microscopy image of a typical device is shown in Figure 1(b).

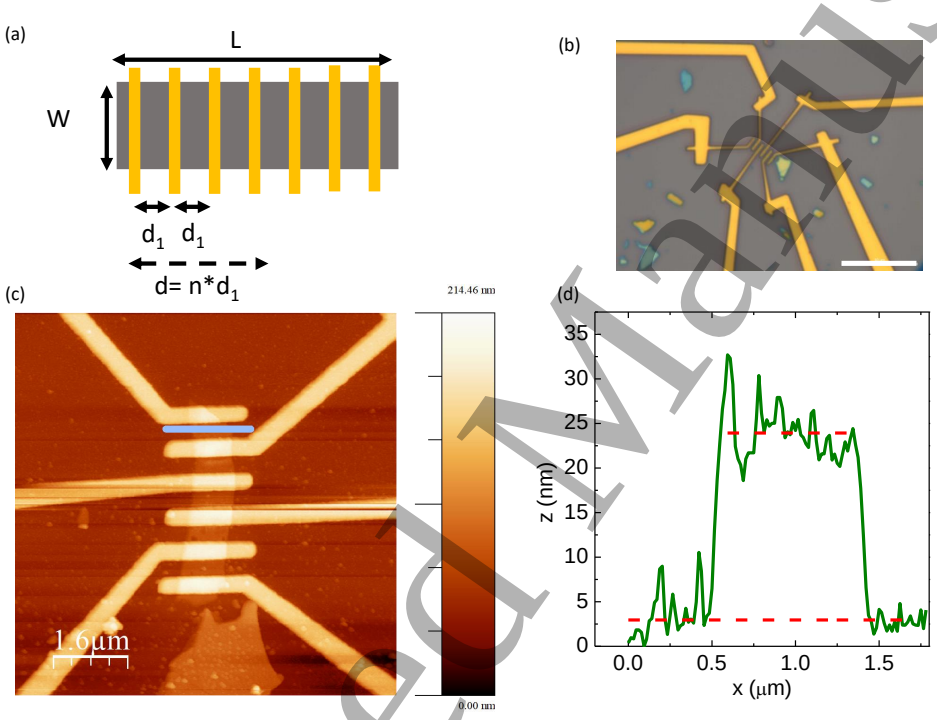

Figure 1. (a) Schematics of the devices for transfer length method. Length (L) and width (W) of the bP flake are indicated. d_1 is the distance between neighboring contacts, while we label the general distance between two contacts as d. (b) Optical microscopy image of device 10. The scale bar is 10 μm. (c) AFM image of the device shown in (b). The scale bar is 1.6 μm. (d) Profile along the line indicated in (c) to measure the flake thickness, which is (21 ± 4) nm. The red dotted lines indicate the average substrate and flake level.

To measure the geometrical parameters of the flakes, after the electrical transport measurements, we removed the protective layer to perform AFM measurements. One example is shown in Figure 1(c). This process was performed as a last characterization step, since an AFM measurement in air degrades the flakes. These measurements allowed to precisely evaluate the width W and length L of the bP flakes and to measure the distances d on each flake. The scattering in d with respect to the nominal value resulted smaller than 5% for all devices. Furthermore, we extracted flake thickness from cross–sections such as the one shown in Figure 1(d). The thickness of the individual flakes is

in the range $15 - 40$ nm, which coincides with the thickness range found in literature on bP contacts [28, 43] and allows a comparison between different devices, since band alignment and Fermi level pinning do not change anymore significantly with thickness in this range [34]. The geometrical dimensions of the individual flakes are presented in the Supplementary Material.

3.2. Electrical characterization

The devices were measured at room temperature and at low temperature (4.2 K). As a standard for the analysis, we used a bias voltage in the ± 1 mV range, which is the one typically used in experiments. In order to evaluate R_2, we acquired a full current–voltage ($I - V$) curve for each pair of contacts and extracted the two–probe resistances from linear fits of these curves. Examples of $I - V$ characteristics are shown in Figure 2(a). The slope of the $I - V$ curves decreases with increasing distance between the electrodes. We found that the $I - V$ behavior of all devices is linear in this bias range, independent of contact metal. The linear behavior of the $I - V$ curves demonstrates the good quality of the contacts. Furthermore, it is crucial for the correct evaluation of the two–probe resistance R_2. Generally the ± 1 mV range is suitable for performing transport measurements, since higher bias voltages could produce self heating in the proximity of contacts due to current crowding [39]. Nevertheless, at low temperature we measured some $I - V$ curves in a wider bias voltage range, namely ± 100 mV. A typical $I - V$ curve in this range for a device of each metal is shown in Figure 2(b).

To quantitatively evaluate the linearity of the $I - V$ curves, we performed a linear fit of each curve and used the adjusted r^2 of the fit as an indicator of the linearity. As can be seen in Figure 2(b), with no gate bias applied ($V_g = 0$ V), all curves are linear, with an adjusted $r^2 \approx 0.99$ or higher. As a first indication, the linear trend of the I-V curves suggests that the energy barrier, if any, at the bP/metal interface is very small for all three metals investigated.

Source–drain current vs. gate voltage measurements are shown in Figure 2(c). These measurements do not show any ambipolar behavior in the ± 80 V range, while they instead show a strong unipolar p–type conduction, independent of the metal used. Several factors could contribute to this effect, such as flake thickness, since we realized our FETs with bP multilayers in the 15 nm to 40 nm thickness range, or the 300 nm thickness of the SiO_2 used as a gate dielectric, which could be too thick to efficiently gate bP into the electron region. Other studies performed with a much thinner SiO_2 [15, 36] or with an even thinner HfO_2 gate [44] successfully reach the electron region. Another factor which could play a role is the oxygen plasma procedure that we use, since, as suggested by some preliminary evidence [43, 63], oxygen exposure could increase the p–type doping of bP. However, a systematic investigation of the link between oxygen exposure and p–type doping is still missing.

Figure 2(c) shows that for positive gate voltage above 40 V, one device (Ti) reaches the depletion regime, highlighted in the inset to Figure 2(c) on a logarithmic scale,

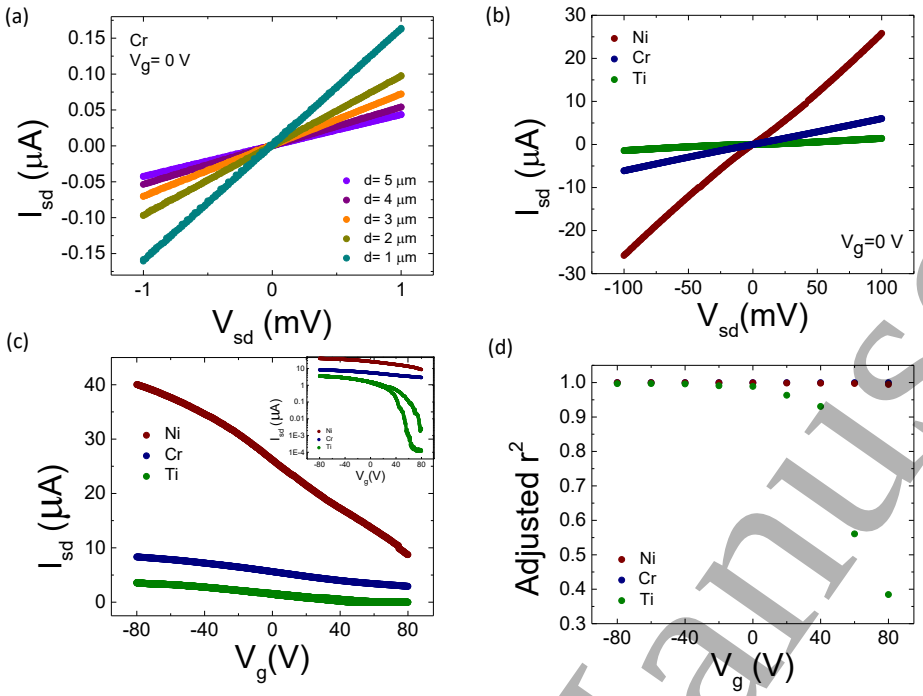

Figure 2. (a) Two–probe current–voltage characteristics for different contact distances d at room temperature in the ± 1 mV bias range for a device with Cr contacts (device 2). Similar measurements for all metals investigated are reported in the Supplementary Material. (b) Two–probe current–voltage characteristics in the ± 100 mV bias range at $T = 4.2$ K (Ni, red curve, device 7; Cr, blue curve, device 3; Ti, green curve, device 6) (c) Source–drain current versus gate voltage for the same devices. $V_{sd} = 100$ mV. The inset shows the same data on a logarithmic scale, which highlights the presence of a hysteresis in the depletion regime. $T = 4.2$ K (d) Adjusted r^2 of the linear fits of all current–voltage measurements acquired at different gate voltages. $T = 4.2$ K.

and shows a hysteresis there. A similar behavior was found for another device (with Ni contacts, see the Supplementary Material), which underlines that this effect is not related to the contact metal type. The hysteresis in bP FETs on SiO_2 has been previously related to trap states at the interface [64].

As a last remark, it has to be noticed that the $I-V$ characteristics in these devices becomes non–linear when the depletion regime is reached. The adjusted r^2 of linear fits to current–voltage measurements at various gate voltages are displayed in Figure 2(d). While in the accumulation regime all contacts show a linear trend (adjusted $r^2 \approx 1$), the adjusted r^2 drops when a device reaches the depletion regime, here $r^2 < 0.8$ for $V_g > 40$ V for the device with Ti contacts. A similar deterioration of contact quality in the depletion regime has already been reported for bP [65].

3.3. Contact resistance

Plots of R_2 vs. d for three representative devices, one for each metal, are presented together with linear fits in Figure 3, both for room temperature (panel (a)) and low temperature (panel (b)). The linear trend expected from TLM is indeed observed, and the scattering of the resistance values for the same distance d is very small, as visible from the error bars, which are often barely visible in the graph. From the slope of the linear fits, the sheet resistance R_S is obtained, while the intercept is equal to $2R_C$. To better inspect this region of interest, a zoom–in at d close to 0 is shown in the insets of Figures 3(a) and (b).

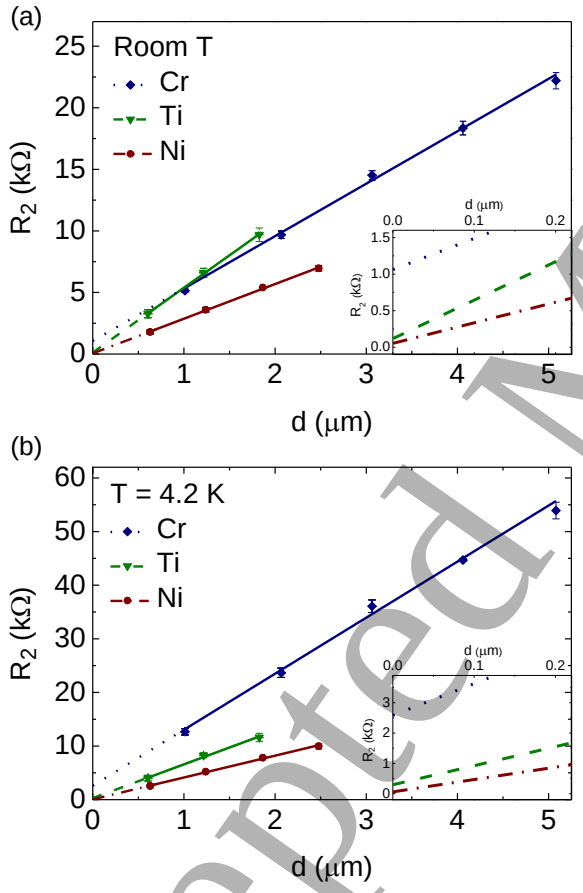

Figure 3. Transfer length method: average two–probe resistance R_2 at room temperature (a) and at low temperature (b) as a function of contact distance d. The solid lines in (a) and (b) are the results of the linear fit procedure. Outside the range of fitting, the same linear function is plotted using dashed lines. A zoom–in showing the intercepts at $d = 0$, corresponding to $2R_C$, is shown in the insets of panels (a) and (b). Ni: device 7, Ti: device 5, Cr: device 2.

We then calculated $R_C \cdot W$ and averaged the results ($\overline{R_C \cdot W}$) for all devices which had contacts of the same metal, in order to rule out as much as possible device–dependent effects and to obtain the general trend related just to the metal bP layer contact. The results are presented in Table 1. Two different errors are evaluated on

the aggregate data: the propagated error on the average, labeled as avg. error, which is related to the experimental errors during the measurements and the scattering of the data on the single device, see Figure 3. The other relevant uncertainty is the standard error, labeled in the table as std. error, which is the standard deviation of the distribution of contact resistances of different devices with the same contact metal divided by $\sqrt{N}$, where N is the number of devices. This latter value allows an evaluation of the scattering between different devices with the same metal. Further information on the evaluation of uncertainties is presented in the Supplementary Material.

		Room T			Low T (4.2 K)		
Metal	Method	$\overline{R_C \cdot W}$ [$\Omega\,\mu$m]	avg. error [$\Omega\,\mu$m]	std. error [$\Omega\,\mu$m]	$\overline{R_C \cdot W}$ [$\Omega\,\mu$m]	avg. error [$\Omega\,\mu$m]	std. error [$\Omega\,\mu$m]
Cr	TLM	797	64	253	2428	198	1377
	R_2 *vs* R_4	444	165	0.2	1353	240	408
Ti	TLM	217	88	163	740	209	282
	R_2 *vs* R_4	484	56	-*	912	225	382
Ni	TLM	135	13	64	432	30	208
	R_2 *vs* R_4	138	25	75	448	64	213

Table 1. Average of the normalized contact resistance $\overline{R_C \cdot W}$ obtained from the TLM measurements and from the comparison between two–probe and four–probe resistances (R_2 *vs* R_4), both at room temperature and at 4.2 K, for each of the three metals investigated. Both the propagated error on the average (avg. error) and the standard error (std. error) are displayed. *: The standard error is missing because these measurements are from a single device.

Figure 3 shows that contact resistance at low temperature is higher than at room temperature, which suggests a contribution of bP to R_C for all three metals. This trend is also clearly visible from the contact resistance data presented in Table 1. At room temperature, $\overline{R_C \cdot W} = 135\ \Omega\,\mu$m is obtained for Ni, which is among the lowest previously reported contact resistances in literature for bP [41, 50, 66], also for the Ni/bP interface [36, 37], and well within the 2017 target for silicon transistors in the International Technology Roadmap for Semiconductors (ITRS) [67]. Ti has a normalized contact resistance which is slightly higher ($\sim 200\ \Omega\,\mu$m), but still much lower than values reported in literature for this metal [15, 47], while the highest contact resistance is obtained for Cr with $\overline{R_C \cdot W} \sim 800\ \Omega\,\mu$m. Also at low temperature, chromium with $\sim 2400\ \Omega\,\mu$m is the metal that shows the highest contact resistance, followed by Ti with $740\ \Omega\,\mu$m. Despite its comparatively lower performance, the normalized contact resistance for Cr contacts at low temperature is still lower than in previous reports [51]. Ni with $430\ \Omega\,\mu$m confirms to be the metal with the lowest contact resistance, with $\overline{R_C \cdot W}$ more than a factor five smaller than for Cr. Moreover, with the lowest scattering of the results, Ni contacts show the most consistent performance among the three metals investigated.

To obtain another independent evaluation of contact resistance, we compared four–probe and two–probe measurements ($R_2 vs R_4$). For this purpose, the outermost contacts were used as source and drain, while all other contact combinations were used for the four–probe resistance measurements (R_4). Four–probe resistance measures just the contribution of the bP channel, $R_4 = R_S \cdot d/W$. We compare this value with the corresponding two–probe resistance $R_2 = 2 \cdot R_C + R_S \cdot d/W = 2 \cdot R_C + R_4$, measured using the same *inner* contacts as for the four–probe measurement. We can thus evaluate R_C as $R_C = (R_2 - R_4)/2$. This method allows to eliminate the influence of any possible inhomogeneity of the bP channel, because the very same region of the channel is probed in both measurements. In these measurements, which are summarized in Table 1, Ni shows again the best performance, with specific contact resistivity values which are consistent with those obtained by TLM. Also for Ti, a good agreement between the two methods is obtained, especially at low temperature, while for Cr comparatively large variations are observed.

Table 1 shows that the standard error is typically larger than the average error. This is expected because the standard error describes the scattering between the different devices and includes therefore the variation in the characteristics of the specific flakes, which were intentionally allowed to vary, such as the thickness or their crystallographic orientation. On this latter aspect it has to be underlined that conductivity varies at most by a factor 1.5 between the armchair and the zigzag direction [18].

Our results for the Ni and Ti contacts are in good agreement with previous studies on SBH. Quhe et al. [31] report for Ni a SBH between 0 eV and 0.36 eV, while Pan et al. [30] report a SBH between 0.02 eV and 0.26 eV. The two different values for SBH are related to longitudinal and transversal injection of the carriers. Also Ti is shown to have a low barrier for hole injection into bP, both from theoretical modeling [32] and from an experiment by Liu et al. [33], in which a SBH of 0.21 eV is obtained. This is consistent with our data, which show that the performance of Ti-contacted devices does not significantly differ from those with Ni contacts. The larger variation in contact resistance for devices with Ti contacts compared to Ni can be explained by the higher reactivity of Ti [68].

From our measurements it appears that the performance of the Cr contacts is moderate, both in terms of contact resistance and for what concerns the scattering from device to device. Therefore, the Schottky–Mott rule does not capture the full physics occurring at this interface. However, it is well known that Fermi level pinning [26] can occur, which leads to a deviation from the ideal trend [69]. The configuration of the surface states in the semiconductor is very important in determining Fermi level pinning [70, 71]. A theoretical prediction suggests a more defected growth of Cr on bP with respect to Ni. From energetic considerations, it appears that a three–dimensional island growth of Cr on bP is favorable, while for Ni a two–dimensional growth is predicted [72]. This different growth mechanism could be relevant here, since defects, interface dipole moments, and the chemistry at the interface can produce significant deviations from the simple Schottky–Mott model [71]. Also the calculations and experimental observations

by Jiang et al. [34] suggest that the Cr/bP interface is not as favorable for hole injection as the Schottky-Mott rule would suggest. Moreover, independent theoretical studies on monolayer bP suggest that at the interface with Cr, non–trivial effects occur, leading to a better transport for electrons than for holes [30].

Table 2 gives the values of sheet resistance R_S obtained from the slope of the linear fits in Figure 3. Besides, we obtain an independent evaluation of sheet resistance from the four–probe measurements, since $R_S = R_4 \cdot W/d$. Data obtained with TLM and R_2 *vs* R_4 methods display both at room and low temperature a very good consistency for all three metals investigated. At room temperature, devices from all three metals have similar sheet resistance. At low temperature, instead, the sheet resistance for Cr–contacted samples increases much more than for the other two metals, reaching 18 kΩ, which is further evidence for an interfacial reaction between Cr and bP. Moreover, the low R_S of the devices with Ni contacts is associated with a higher mobility in these devices at low temperature, as shown in the Supplementary Material. Since for thin flakes the scattering at the interfaces is relevant, and since a significant amount of the device area is covered by contacts, we can ascribe this increased mobility to a higher quality of the Ni/bP interface with respect to the other metals.

Metal	Method	Room T, $\overline{R_s}$ [kΩ]	Low T (4.2 K), $\overline{R_s}$ [kΩ]
Cr	TLM	7.5 ± 1.4	17.3 ± 8.0
	R_2 *vs* R_4	6.5 ± 0.7	18.0 ± 9.0
Ti	TLM	7.0 ± 1.5	9.3 ± 2.0
	R_2 *vs* R_4	7.0 ± 1.4	9.8 ± 2.6
Ni	TLM	4.9 ± 1.5	5.8 ± 1.0
	R_2 *vs* R_4	4.8 ± 1.5	5.7 ± 0.9

Table 2. Average sheet resistance of bP for three contact metals. Only the larger between avg. error and std. error is shown in the table for clarity.

From the gate voltage modulation, combined with R_S, we can calculate the carrier concentration n of each device using the Drude model. A cross-check of these results with an evaluation of n from the threshold voltages gives consistent carrier concentrations, as described in detail in the Supplementary Material. We then investigate if there is a correlation between R_C and carrier concentration in the individual devices, and compare our results with the quantum limit [9]. These data are reported in Figure 4. There is a trend of R_C with carrier concentration. Nevertheless, the scattering between the different devices suggests that band alignment is not the only relevant contribution to R_C, and that other effects such as the chemistry at the interface play an important role. Furthermore, R_C approaches the quantum limit [9] in a wide range of carrier concentrations, both for devices with Ni and Ti contacts.

Surprisingly, the correlation of contact resistance with carrier density for bP is difficult to retrieve in literature. In order to compare our results with previous

reports, we added in Figure 4 literature data for Ti at room temperature [42], Pt at room temperature [40], and Cr at low temperature [51]. Details are reported in the Supplementary Material. Clearly, our best devices show a superior performance both with respect to other studies on bP [36, 42, 44, 51, 52, 53] and also in comparison to other 2D materials [73].

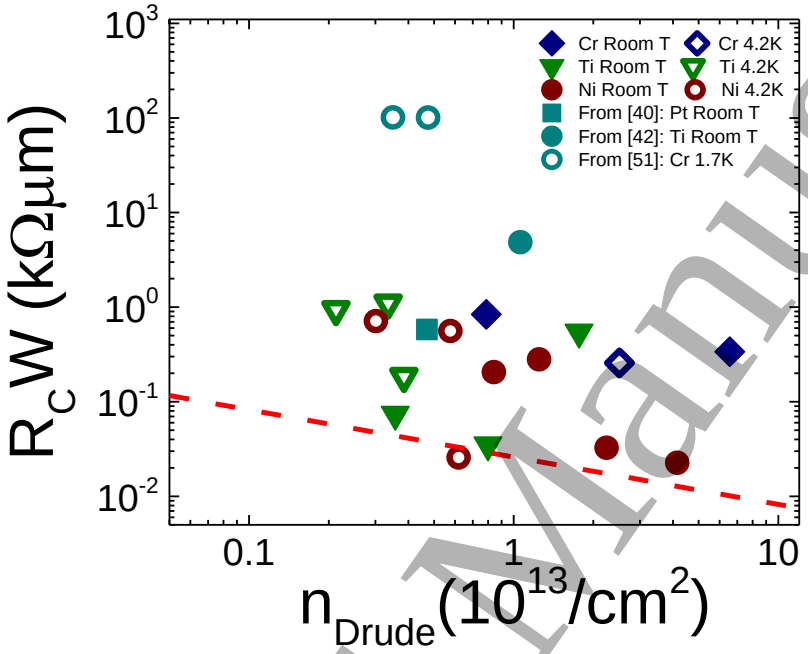

Figure 4. Contact resistance of the individual devices versus carrier concentration. For clarity, only TLM values of R_C are used, and error bars are not displayed. The full symbols represent room temperature data, while the empty symbols represent low temperature data. Cr is associated with blue, Ti with green, and Ni with red symbols. Data from literature are included, using a full square for Yang et al. [40], a full circle for Das et al. [42], and empty circles for Chen et al. [51]. The quantum limit is displayed as a dashed line.

4. Conclusions

In this work, we presented a study of contact resistance in exfoliated black phosphorus devices with thickness $15 - 40$ nm in a transfer length method configuration. Three different metals, Titanium, Chromium, and Nickel were used, and measurements were performed both at room temperature and at liquid Helium temperature. In order to evaluate how robust the observed trends are, we presented aggregate data from 10 devices and used two different exfoliation protocols for bP.

Both at room temperature and at low temperature, contacts from all three metals show linear $I - V$ curves in the ± 1 mV regime. In all samples we observed a strong unipolar p–type behavior. We observe a linear behavior for all three metals in the

±100 mV bias voltage regime, except when the depletion regime is reached and I_{sd} approaches zero, as previously already observed in bP FETs [65].

Devices contacted with Cr display the highest contact resistances and the largest scattering of the data. The anomalous behavior of Cr–contacted devices can be related to a more defective growth mechanism of Cr on bP, consistent with theoretical studies [72]. The lowest $\overline{R_C W}$ is obtained for Ni contacts, which also display the smallest scattering among the different devices both at room temperature and at low temperature. This trend is confirmed by the comparison between two–probe and four–probe resistance measurements.

These results suggest that the quality of the bP/metal interface plays a crucial role in lowering contact resistance. Moreover, by demonstrating a correlation of $R_C W$ with carrier concentration, we clearly show that our best devices, both with Ni and Ti contacts, approach the quantum limit for a broad range of carrier concentrations.

Acknowledgments

The authors would like to thank Alessandra Campana for her support during the initial stage of this work. This work was financially supported by EC through the project PHOSFUN *Phosphorene functionalization: a new platform for advanced multifunctional materials* (ERC ADVANCED GRANT No. 670173 to M. P.). S. H. thanks Scuola Normale Superiore for support, project SNS16_B_HEUN – 004155. F. T. thanks CNR–Istituto Nanoscienze for funding the SEED project 2017 SURPHOS.

References

[1] Allain A, Kang J, Banerjee K and Kis A 2015 *Nature Materials* **14** 1195–1205
[2] Léonard F and Talin A A 2011 *Nature Nanotechnology* **6** 773–783
[3] Choi M S, Lee S H and Yoo W J 2011 *Journal of Applied Physics* **110** 073305
[4] Song S M and Cho B J 2013 *Carbon Letters* **14** 162–170
[5] Wang L, Meric I, Huang P Y, Gao Q, Gao Y, Tran H, Taniguchi T, Watanabe K, Campos L M, Muller D A, Guo J, Kim P, Hone J, Shepard K L and Dean C R 2013 *Science* **342** 614–617
[6] Kappera R, Voiry D, Yalcin S E, Branch B, Gupta G, Mohite A D and Chhowalla M 2014 *Nature Materials* **13** 1128–1134
[7] Kappera R, Voiry D, Yalcin S E, Jen W, Acerce M, Torrel S, Branch B, Lei S, Chen W, Najmaei S, Lou J, Ajayan P M, Gupta G, Mohite A D and Chhowalla M 2014 *APL Materials* **2** 092516
[8] Cho S, Kim S, Kim J H, Zhao J, Seok J, Keum D H, Baik J, Choe D H, Chang K J, Suenaga K, Kim S W, Lee Y H and Yang H 2015 *Science* **349** 625–628
[9] Jena D, Banerjee K and Xing G H 2014 *Nature Materials* **13** 1076–1078
[10] Giannazzo F, Fisichella G, Piazza A, Di Franco S, Greco G, Agnello S and Roccaforte F 2016 *Physica Status Solidi - Rapid Research Letters* **10** 797–801
[11] Giannazzo F, Fisichella G, Greco G, Di Franco S, Deretzis I, La Magna A, Bongiorno C, Nicotra G, Spinella C, Scopelliti M, Pignataro B, Agnello S and Roccaforte F 2017 *ACS Applied Materials & Interfaces* **9** 23164–23174
[12] Wang Y, Kim J C, Wu R J, Martinez J, Song X, Yang J, Zhao F, Mkhoyan A, Jeong H Y and Chhowalla M 2019 *Nature* **568** 70–74
[13] Morita A 1986 *Applied Physics A Solids and Surfaces* **39** 227–242

[14] Castellanos-Gomez A, Vicarelli L, Prada E, Island J O, Narasimha-Acharya K L, Blanter S I, Groenendijk D J, Buscema M, Steele G A, Alvarez J V, Zandbergen H W, Palacios J J and van der Zant H S J 2014 *2D Materials* **1** 025001

[15] Das S, Zhang W, Demarteau M, Hoffmann A, Dubey M and Roelofs A 2014 *Nano Letters* **14** 5733–5739

[16] Castellanos-Gomez A 2015 *Journal of Physical Chemistry Letters* **6** 4280–4291

[17] Long G, Maryenko D, Shen J, Xu S, Hou J, Wu Z, Wong W K, Han T, Lin J, Cai Y, Lortz R and Wang N 2016 *Nano Letters* **16** 7768–7773

[18] Xia F, Wang H and Jia Y 2014 *Nature Communications* **5** 4458

[19] Lee S, Yang F, Suh J, Yang S, Lee Y, Li G, Sung Choe H, Suslu A, Chen Y, Ko C, Park J, Liu K, Li J, Hippalgaonkar K, Urban J J, Tongay S and Wu J 2015 *Nature Communications* **6** 8573

[20] Hemsworth N, Tayari V, Telesio F, Xiang S, Roddaro S, Caporali M, Ienco A, Serrano-Ruiz M, Peruzzini M, Gervais G, Szkopek T and Heun S 2016 *Physical Review B* **94** 245404

[21] Telesio F, Hemsworth N, Dickerson W, Petrescu M, Tayari V, Yu O, Graf D, Serrano-Ruiz M, Caporali M, Peruzzini M, Carrega M, Szkopek T, Heun S and Gervais G 2019 *Physica Status Solidi (RRL) – Rapid Research Letters* 1900347

[22] Favron A, Gaufrès E, Fossard F, Phaneuf-L'Heureux A L, Tang N Y W, Lévesque P L, Loiseau A, Leonelli R, Francoeur S and Martel R 2015 *Nature Materials* **14** 826–832

[23] Huang Y, Qiao J, He K, Bliznakov S, Sutter E, Chen X, Luo D, Meng F, Su D, Decker J, Ji W, Ruoff R S and Sutter P 2016 *Chemistry of Materials* **28** 8330–8339

[24] Luo W, Zemlyanov D Y, Milligan C A, Du Y, Yang L, Wu Y and Ye P D 2016 *Nanotechnology* **27** 434002

[25] Ahmed T, Balendhran S, Karim M N, Mayes E L H, Field M R, Ramanathan R, Singh M, Bansal V, Sriram S, Bhaskaran M and Walia S 2017 *npj 2D Materials and Applications* **1** 18

[26] Schroder D K 2006 *Semiconductor Material and Device Characterization* (Wiley-IEEE Press)

[27] Sze S 1969 *Physics of Semiconductor Devices* (Wiley)

[28] Cai Y, Zhang G and Zhang Y W 2014 *Scientific Reports* **4** 6677

[29] Gong K, Zhang L, Ji W and Guo H 2014 *Phyical Reiew B* **90**(12) 125441

[30] Pan Y, Wang Y, Ye M, Quhe R, Zhong H, Song Z, Peng X, Yu D, Yang J, Shi J and Lu J 2016 *Chemistry of Materials* **28** 2100–2109

[31] Quhe R, Wang Y, Ye M, Zhang Q, Yang J, Lu P, Lei M and Lu J 2017 *Nanoscale* **9** 14047–14057

[32] Quhe R, Peng X, Pan Y, Ye M, Wang Y, Zhang H, Feng S, Zhang Q, Shi J, Yang J, Yu D, Lei M and Lu J 2017 *ACS Applied Materials and Interfaces* **9** 3959–3966

[33] Liu H, Neal A T, Zhu Z, Luo Z, Xu X, Tománek D and Ye P D 2014 *ACS Nano* **8** 4033–4041

[34] Jiang B, Zou X, Su J, Liang J, Wang J, Liu H, Feng L, Jiang C, Wang F, He J and Liao L 2018 *Advanced Functional Materials* **28** 1801398

[35] Li X, Grassi R, Li S, Li T, Xiong X, Low T and Wu Y 2018 *Nano Letters* **18** 26–31

[36] Du Y, Liu H, Deng Y, Ye P D and Peide D Y 2014 *ACS Nano* **8** 10035–10042

[37] Ling X, Wang H, Huang S, Xia F, Dresselhaus M S and Lau J 2015 *PNAS* **112** 4523

[38] Avsar A, Tan J Y, Luo X, Khoo K H, Yeo Y, Watanabe K, Taniguchi T, Quek S Y and Özyilmaz B 2017 *Nano Letters* **17** 5361–5367

[39] Wang Q, Tao X, Yang L and Gu Y 2016 *Applied Physics Letters* **108** 103109

[40] Yang L M, Qiu G, Si M W, Charnas A R, Milligan C A, Zemlyanov D Y, Zhou H, Du Y C, Lin Y M, Tsai W, Paduano Q, Snure M and Ye P D 2017 *International Electron Devices Meeting, IEDM* **7** 5.5.1–5.5.4

[41] Ma Y, Shen C, Zhang A, Chen L, Liu Y, Chen J, Liu Q, Li Z, Amer M R, Nilges T, Abbas A N and Zhou C 2017 *ACS Nano* **11** 7126–7133

[42] Das S, Demarteau M and Roelofs A 2014 *ACS Nano* **8** 11730–11738

[43] Perello D J, Chae S H, Song S and Lee Y H 2015 *Nature Communications* **6** 7809

[44] Haratipour N, Robbins M C and Koester S J 2015 *IEEE Electron Device Letters* **36** 411–413

[45] Li L, Engel M, Farmer D B, Han S J and Wong H S 2016 *ACS Nano* **10** 4672–4677

[46] Liu H, Neal A T, Zhu Z, Luo Z, Xu X, Tomanek D and Ye P D 2014 *ACS Nano* **8** 4033–4041
[47] Haratipour N, Namgung S, Grassi R, Low T, Oh S H and Koester S J 2017 *IEEE Electron Device Letters* **38** 685–688
[48] Haratipour N, Liu Y, Wu R J, Namgung S, Ruden P P, Mkhoyan K A, Oh S H and Koester S J 2018 *IEEE Transactions on Electron Devices* **65** 4093–4101
[49] Li Y, Lin S, Liu Y, Chai Y and Lau S P 2019 *2D Materials* **6** 024001
[50] Park H, Son J and Kim J 2018 *Journal of Materials Chemistry C* **6** 1567–1572
[51] Chen X, Wu Y, Wu Z, Xu S, Wang L, Han Y, Han T, He Y, Cai Y and Wang N 2015 *Nature Communications* **6** 7315
[52] Ling Z P, Sakar S, Mathew S, Zhu J T, Gopinadhan K, Venkatesan T and Ang K W 2015 *Scientific Reports* **5** 18000
[53] Du Y, Yang L, Zhou H and Ye P D 2016 *2016 International Symposium on VLSI Technology, Systems and Application, VLSI-TSA 2016* **21** 9–10
[54] Lide D R 2008 *Handbook of Chemistry and Physics* (CRC Press/Taylor and Francis)
[55] Feng Q, Yan F, Luo W and Wang K 2016 *Nanoscale* **8** 2686–2692
[56] Tung R T 1993 *Journal of Vacuum Science & Technology B: Microelectronics and Nanometer Structures* **11** 1546–1552
[57] Lee S Y, Yun W S and Lee J D 2017 *ACS Applied Materials and Interfaces* **9** 7873–7877
[58] Köpf M, Eckstein N, Pfister D, Grotz C, Krüger I, Greiwe M, Hansen T, Kohlmann H and Nilges T 2014 *Journal of Crystal Growth* **405** 6–10
[59] Dickerson W, Tayari V, Fakih I, Korinek A, Caporali M, Serrano-Ruiz M, Peruzzini M, Heun S, Botton G A and Szkopek T 2018 *Applied Physics Letters* **112** 173101
[60] Tayari V, Hemsworth N, Fakih I, Favron A, Gaufrès E, Gervais G, Martel R and Szkopek T 2015 *Nature Communications* **6** 7702
[61] Telesio F, Passaglia E, Cicogna F, Costantino F, Serrano-Ruiz M, Peruzzini M and Heun S 2018 *Nanotechnology* **29** 295601
[62] Horcas I, Fernández R, Gómez-Rodríguez J M, Colchero J, Gómez-Herrero J and Baro A M 2007 *Review of Scientific Instruments* **78** 013705
[63] Doganov R A, O'Farrell E C T, Koenig S P, Yeo Y, Ziletti A, Carvalho A, Campbell D K, Coker D F, Watanabe K, Taniguchi T, Castro Neto A H and Özyilmaz B 2015 *Nature Communications* **6** 6647
[64] Illarionov Y Y, Waltl M, Rzepa G, Kim J S, Kim S, Dodabalapur A, Akinwande D and Grasser T 2016 *ACS Nano* **10** 9543–9549
[65] Li L, Yu Y, Ye G J, Ge Q, Ou X, Wu H, Feng D, Chen X H and Zhang Y 2014 *Nature Nanotechnology* **9** 372–377
[66] Huang H, Jiang B, Zou X, Zhao X and Liao L 2019 *Science Bulletin* **64** 1067–1079
[67] Liu Y, Guo J, Wu Y, Zhu E, Weiss N O, He Q, Wu H, Cheng H C, Xu Y, Shakir I, Huang Y and Duan X 2016 *Nano Letters* **16** 6337–6342
[68] Chang H M, Fan K L, Charnas A, Ye P D, Lin Y M, Wu C I and Wu C H 2018 *Journal of Physics D: Applied Physics* **51** 135306
[69] Wang C H, Incorvia J A C, McClellan C J, Yu A C, Mleczko M J, Pop E and Wong H S P 2018 *Nano Letters* **18** 2822–2827
[70] Bardeen J 1947 *Physical Review* **71** 717–727
[71] Tung R T 2014 *Applied Physics Reviews* **1** 011304
[72] Hu T and Hong J 2015 *Journal of Physical Chemistry C* **119** 8199–8207
[73] Liu Y, Duan X, Huang Y and Duan X 2018 *Chemical Society Reviews* **47** 6388–6409